Sensitivity Study on Interfacial Closure Laws in Two-Fluid Bubbly Flow Simulations

R. S. Oey, R. F. Mudde and H. E. A. van den Akker
Delft University of Technology, Kramers Laboratorium voor Fysische Technologie,
2628 BW Delft, The Netherlands

The two-fluid formulation with closure models for interfacial forces and turbulence is applied to the evaluation of a meandering plume in a rectangular bubble column. In literature there is some discussion about how precisely the models should be in order to capture the dynamics as is observed experimentally. Furthermore, this type of flow has shown to be quite sensitive for the degree of diffusion (physical and numerical) introduced in the model equations. The focus is on the necessity and influence of certain interfacial closure models in above type of bubbly flow. The influence of the drag, turbulent diffusive, and added mass force will be highlighted. TVD schemes are used for the computations to obtain accurate results against low costs, that is, coarse grid approximation and to reduce the amount of numerical diffusion as much as possible. Still these schemes have to be "tuned" in their properties in order to obtain the desired accuracy. Nonproper choice of certain parameters, that is, "flux-limiters" introduces errors in the final solution, with the same order of magnitude as physical phenomenon, which are introduced by interfacial forces.

Introduction

Computational Fluid Dynamics (CFD) has gained much popularity for the prediction of dynamics of bubbly flows in industrial types of reactors. This class of flows is difficult to model since they are time-dependent, turbulent, and in the dense gas phase region. Although there are several ways for modeling the hydrodynamics of these flows, it is the Euler-Euler based, two-fluid formulation which is in favor when it comes to predicting bubbly flows on industrial scales, with today's available computational power. The concept of the two-fluid formulation is that both phases (gas and liquid) are treated as interpenetrating continua, represented by sets of mass and momentum balances.

Several publications have appeared lately on the modeling and simulation of bubbly flows based on an Euler-Euler type of approach (Lahey, 1990; Sokolichin and Eigenberger, 1994; Celik and Wang, 1994; Grevskott et al. 1996; Jakobsen et al., 1997; Ranade, 1997; Dudukovic et al., 1999; Krishna et al., 1999; Jakobsen, 2001; Mudde and Simonin, 1999; Pfleger et al., 1999; Sokolichin and Eigenberger, 1999; Ranade and Utikar, 1999; Pan et al., 2000; Oey et al., 2001; Pfleger and Becker, 2001). These studies have revealed two important issues on capturing the correct dynamics of the flow using CFD. The first issue is that in order to capture the transient nature of bubbly flows, as has been observed experimentally, a two-dimensional (2-D) CFD model is not sufficient (Sokolichin and Eigenberger, 1994, 1999; Mudde and Simonin, 1999). The model has to be 3-D. The reason lies in the fact that in 2-D simulations one overestimates the turbulent viscosity in the turbulence models. In this way the momentum equations of the two-fluid formulation become more or less diffusion dominated and dampens, if not completely suppresses, time-dependent solutions.

The second important issue, which was explicitly stated by Sokolichin and Eigenberger (1999), is in the approximation of convective transport. The main problem in approximating convection is to combine accuracy, stability, economy and algebraic simplicity. In principle convection may be discretized by using central difference schemes because of second-order accuracy. However, if the mesh Peclet number is too large, nonphysical numerical oscillations, called "wiggles," may occur, impairing accuracy and stability. In order to avoid the instability and nonmonotonicity in the numerical solution,

Correspondence concerning this article should be addressed to R. S. Oey.

first-order upwind is often used. Unfortunately, this method introduces excessive numerical diffusion, acting like an artificial viscosity. In high-Reynolds-number flow, this numerical diffusion dominates the physical diffusion in such a way that it smoothens the solution and suppresses the transient character of the flow. Sokolichin and Eigenberger (1999) did not use a full two-fluid approach for the hydrodynamics. Instead, they modeled the continuous phase by the Navier-Stokes equations with a source term accounting for the interaction with the gas phase. The velocity difference between the dispersed phase and the continuous phase is assumed equal to a slip velocity and a drift velocity. Essentially, this is equivalent to neglecting all terms in the momentum equations of the dispersed phase, except the interfacial forces and the gravitational forces. Hence, only a mass balance equation for the dispersed phase has to be solved. In the present study, as in the study done by Mudde and Simonin (1999), a full two-fluid approach is used.

The improvement of accuracy can traditionally be done by grid refinement. However, particularly in 3-D applications, grid refinement is not always possible, due to excessive storage and run time requirement. Also, grid refinement reduces the stability of the computations due to the reduction of numerical diffusion. A way to circumvent these problems is the introduction of high-resolution Total Variation Diminishing (TVD) schemes for the approximation of convective transport. Since the work of Harten (1983), a rigorous mathematical foundation has been laid for this type of scheme. A comprehensive collection of all important articles regarding this subject can be found in Hussaini et al. (1997). These schemes have still the stability property of first-order upwind, are monotone (do not introduce "wiggles"), are easy to implement in existing codes, while providing a higher-order accuracy. The latter has been shown to be quite important in our 3-D simulations to obtain time-dependent solutions and to analyze the effect of different closure models.

The two main objectives of this article are, first, to study the performance of two sets of different (interfacial) closure models in a particular flow geometry; secondly, to analyze the sensitivity of time-dependent solutions in 3-D bubbly flow simulations with respect to numerical accuracy. The full two-fluid model will be described together with its two closure problems: modeling the interfacial momentum transfer and turbulence phenomena. The model equations are implemented in our in-house code ESTEEM and tested on their performance in a particular flow geometry. The computational setup together with some characteristics of the flow geometry will be outlined. Several simulation results with the two sets of models are presented. Also, the effect of drag, turbulent diffusion, and added mass will be discussed. The sensitivity of the simulations on numerical diffusion will be treated, followed in the final section by conclusions and recommendations.

Mathematical Modeling

Two-fluid formulation

The equations of the two-fluid formulation are derived by ensemble averaging the local instantaneous equations of single-phase flow and their jump-conditions (Delhaye, 1974; Drew, 1983; Zhang and Prosperetti, 1997; Drew and Passman, 1999). Two sets of balance equations for mass, momentum, and energy are obtained. When assuming the flow to be isothermal and ignoring interfacial mass transfer, the energy equations can be skipped and no source or diffusion terms appear in the mass balances. The conservation equations for mass and momentum can be written in the following generic form

Table 1. Variables in Two-Fluid Balance Equations

Balance	Ψ_k	J_k	f_k
Mass	1	0	0
Momentum	$\boldsymbol{v}_k$	$\tau_k + \tau_k^{Re}$	$-\alpha_k \nabla P + \alpha_k \rho_k \boldsymbol{g} + \boldsymbol{M}_k$

$$\frac{\partial \alpha_k \rho_k \Psi_k}{\partial t} + \nabla \cdot \alpha_k \rho_k \boldsymbol{v}_k \Psi_k = \nabla \cdot \alpha_k \boldsymbol{J}_k + f_k \qquad (1)$$

Where k refers to the phase ($k = 1$, continuous phase and $k = 2$, the dispersed phase). α_k denotes the volume fraction, ρ_k denotes the density, and $\boldsymbol{v}_k$ denotes the velocity. Table 1 shows the variables present in the mass and momentum conservation equations.

The molecular stresses and turbulent stresses are represented by τ_k and τ_k^{Re}, respectively. Finally, the pressure, gravitational vector, and interfacial momentum transfer are given by P, $\boldsymbol{g}$ and $\boldsymbol{M}_k$, respectively. Note that the pressure in both phases is the same. Closure is needed for the turbulent stresses τ_k^{Re} and the interfacial momentum transfer $\boldsymbol{M}_k$. The first one will be treated in the next section while the latter one will be treated in a later section.

Modeling of turbulence

Continuous Phase

When the flow is assumed to be isotropic turbulent, the well-known Boussinesq approximation is adopted to model the turbulent stresses in the continuous liquid phase. The following holds in the two-fluid system

$$\tau_1^{Re} = \mu_1^t \left(\nabla \boldsymbol{v}_1 + \nabla \boldsymbol{v}_1^T - \frac{2}{3} \nabla \cdot \boldsymbol{v}_1 \delta_{ij} \right) - \frac{2}{3} \rho_1 k_1 \delta_{ij} \qquad (2)$$

Where μ_1^t is the turbulent or so-called eddy-viscosity and given by

$$\mu_1^t = \rho_1 C_\mu \frac{k_1^2}{\epsilon_1} \qquad (3)$$

The constant C_μ is, as in the case of single-phase turbulent flow, set to 0.09. The first two terms between brackets in Eq. 2 represents the mean strain rate tensor, while the third term accounts for the compressibility effects (Tennekes and Lumley, 1972). The fourth and last term is the turbulent kinetic energy and is determined by solving a, for a two-phase flow adopted, single phase k-ϵ model. The turbulence equations can again be written in the generic form as Eq. 1. Table 2 shows the variables for the model, where ϵ_1 is the turbulence dissipation. The turbulent and molecular viscosity are denoted by μ_1^t and μ_1, respectively. The coefficients $\sigma_{k_1}, \sigma_{\epsilon_1}, C_{\epsilon_1}$

Table 2. Variables in k and ϵ Equation

Ψ_1	J_1	f_1
k_1	$\left(\frac{\mu_1^t}{\sigma_{k_1}}+\mu_1\right)\nabla k_1$	$\alpha_1\rho_1(P_{k_1}-\epsilon_1)+\Pi_{k_1}$
ϵ_1	$\left(\frac{\mu_1^t}{\epsilon_{\epsilon_1}}+\mu_1\right)\nabla\epsilon_1$	$\alpha_1\rho_1\frac{\epsilon_1}{k_1}(C_{\epsilon,1}P_{k_1}-C_{\epsilon,2}\epsilon_1)+\Pi_{\epsilon_1}$

Table 3. Two Different Sets for Π_{k_1} and Π_{ϵ_1}

Model	Π_{k_1}	Π_{ϵ_1}
ψ_G	$2\alpha_2\rho_1F_{D_G}(C_t-1)k_1-\frac{\mu_1^t}{\alpha_1\alpha_2\rho_1\sigma}F_{D_G}(\boldsymbol{v}_2-\boldsymbol{v}_1)\cdot\nabla\alpha_2$	$2\alpha_2\rho_1F_{D_G}(C_t-1)\epsilon_1$
ψ_S	$\frac{\rho_2}{\rho_2+C_a\rho_1}\alpha_2\rho_1F_{D_S}(q_{12}-2k_1+\boldsymbol{V}_d\cdot\boldsymbol{V}_r)$	$C_{\epsilon,3}\frac{\epsilon_1}{k_1}\Pi_{k_1}$

and C_{ϵ_2} are model constants, and have the same values as in single-phase flow (as will be shown in Table 5).

The additional terms Π_{k_1} and Π_{ϵ_1} account for the effects the interfaces have on the continuous-phase turbulence. In multiphase literature one can find several relations for these terms. In the present study two different sets are analyzed. The first set for Π_{k_1} and Π_{ϵ_1} is due to Issa and Oliveira (1993) (see also Gosman et al. (1992)) and will be denoted further as model ψ_G. The second set, denoted as model ψ_S, is based on the work of Bel F'dhila and Simonin (1992) and Elgobashi and Abou-Arab (1983). Both sets are given in Table 3 and will be outlined in the following.

In model ψ_G, F_{DG} is the coefficient of the drag force and σ is a model constant, which is set equal to 1.0. The coefficient C_t represents the ratio of dispersed phase velocity fluctuations to that of the continuous phase, which are taken to be directly proportional to each other. This assumption is a cornerstone in the modeling of two-phase turbulence in model approach ψ_G. Various formulations of C_t and their effects were discussed by Issa and Oliveira (1993). They proposed the following model for C_t

$$C_t=\frac{3+\beta}{1+\beta+2\rho_2/\rho_1} \tag{4}$$

with

$$\beta=\frac{12\alpha_2\rho_1F_{D_G}}{\pi d_b\mu_1}\left(\frac{l_e}{d_b}\right)^2\frac{1}{Re_t},\qquad Re_t=\frac{\rho_1\sqrt{\frac{2}{3}k_1}l_e}{\mu_1}$$

$$l_e=\frac{k_1^{3/2}}{\epsilon_1} \tag{5}$$

where d_b is the mean bubble diameter, Re_t is an eddy Reynolds number, and l_e is a characteristic eddy length scale. Note that the eddy Reynolds number can be written as the ratio of the continuous-phase turbulent viscosity and the molecular viscosity.

Model ψ_S has a more complicated form: the interaction terms are derived rigorously by considering the equation of motion of a single bubble and rewrite this equation again in terms of the fluid velocity (Bel F'dhila and Simonin, 1992) and its correlation. A consequence is that both the coefficient for the drag force, F_{D_S} and the added mass coefficient C_a arise in the formulation. Other quantities arising in the formulation are the fluid-bubble velocity covariance of the dispersed phase q_{12}, the drift velocity $\boldsymbol{V}_d$, and the relative velocity $\boldsymbol{V}_r$, between the two phases (see below).

Dispersed Phase

While in model ψ_G the gas phase is assumed laminar, model ψ_S assumes the gas-phase turbulent. Assuming steady and homogeneous fluid turbulence, Tchen's theory (Tchen, 1947; Simonin, 1990; Viollet and Simonin, 1994) is extended to predict turbulence in the dispersed phase. No extra transport equations have to be solved as in the case of the continuous phase. Instead, a set of algebraic relations couples the dispersed phase turbulence relations to those of the continuous phase. In summary, there are three time scales of importance in this algebraic model that characterize the interaction between the fluctuating motions: first, the characteristic time of the energetic turbulent eddies, τ_1^t; secondly, the characteristic time of bubble entrainment by the fluid motion, or bubble relaxation time τ_{12}^F. The last characteristic time is given by τ_{12}^t, the eddy-bubble interaction time. The time scales play an important role in the determination of the turbulent interaction terms, shown in Table 3, and are given by

$$\tau_1^t=\frac{3}{2}C_\mu\frac{k_1}{\epsilon_1}\qquad \tau_{12}^F=\frac{1}{F_{D_S}}\left(\frac{\rho_2}{\rho_1}+C_a\right)$$

$$\tau_{12}^t=\frac{\tau_1^t}{\sigma_\alpha}\left[1+C_\beta\zeta_r^2\right]^{-1/2} \tag{6}$$

where σ_α is a model constant. The parameter C_β relates to the Lagrangian over Eulerian characteristic length scale ratio, and comparison with experimental results leads to a practical value (Wells and Stock, 1983) of $C_\beta=0.45$ in the direction parallel to the mean relative velocity and $C_\beta=1.80$ in the orthogonal directions. The ratio between the characteristic time of the energetic turbulent eddies and the characteristic bubble entrainment by the continuous fluid motion is given by ζ.

$$\zeta_r=\frac{|\boldsymbol{v}_r|}{\sqrt{(2/3)k_1}} \tag{7}$$

The turbulent kinetic energy k_2 and fluid-bubble velocity covariance of the dispersed phase q_{12} appear in several physical quantities, like the drifting velocity $\boldsymbol{V}_d$, the relative velocity $|\boldsymbol{v}_r|$ and the turbulent interaction terms. The quantities k_2 and q_{12} are expressed in terms of turbulence quantities of the continuous phase and the three time scales as follows

$$k_2=\frac{b^2+\eta_r}{1+\eta_r}k_1\qquad q_{12}=\frac{b+\eta_r}{1+\eta_r}2k_1$$

$$\eta_r=\frac{\tau_{12}^t}{\tau_{12}^F}\qquad b=\frac{1+C_a}{\rho_2/\rho_1+C_a} \tag{8}$$

Interfacial Momentum Transfer

The interfacial forces, denoted by M_k, is a sum of forces associated with drag, added mass, turbulent diffusion, pressure fluctuations, lift, and the Basset forces. Although the lift force (Auton, 1987) has been applied in 2-D studies of gas-liquid flows, it has been often omitted in the small number of 3-D studies for bubbly flows in the two-fluid formalism. The main reason for this is the lack of understanding about the complex mechanism of lift forces in 3-D gas-liquid flows (Bunner and Tryggvason, 1999). However, in a recent article by Sankaranarayanan and Sundaresan (2002), it was shown that the lift force can be of high importance in the stability of 3-D gas-liquid flows and peculiar results like negative lift coefficients can all be explained well. Also, the Basset force is often excluded and assumed negligible. This makes the model and model implementation in CFD-codes less complicated and still appropriate for a broad range of flows.

In this study two different sets of models for drag, added mass, and turbulent diffusion have been used, whereas the lift and Basset force are excluded for reasons already mentioned. Also, the effects of pressure forces, apart from the pressure gradient, have not been accounted for in the present study. The first model set is mainly due to Gosman et al. (1992), while the second model is due to Viollet and Simonin (1994). In the following, they will be denoted by model ω_G and ω_S, respectively.

The drag force, which in magnitude is the largest interfacial force, is attributed to the steady effects and is usually given in terms of a dimensionless drag coefficient C_D. The drag force is specified for both approaches in Table 4. The coefficients for the drag force for model ω_G and ω_S are given by F_{D_G} and F_{D_S}, respectively. They are defined as follows

$$F_{D_G} = \frac{3}{4}\frac{C_D}{d_b}|\boldsymbol{v}_2 - \boldsymbol{v}_1|, \quad F_{D_S} = \frac{3}{4}\frac{C_D}{d_b}|\boldsymbol{v}_r| \tag{9}$$

In the present study the empirical drag coefficient relation by Wen and Yu (1966) for rigid spheres has been used, namely

$$C_D = \frac{24}{Re}(1+0.15Re^{0.687})\,\alpha_1^{-1.7}, \qquad Re < 1000$$
$$C_D = 0.44, \qquad Re \geq 1000 \tag{10}$$

with the corresponding bubble Reynolds number definition

$$Re_G = \frac{\alpha_1\,\rho_1|\boldsymbol{v}_2 - \boldsymbol{v}_1|d_b}{\mu_1}, \qquad Re_S = \frac{\alpha_1\,\rho_1|\boldsymbol{v}_r|d_b}{\mu_1} \tag{11}$$

Again d_b, as it appears in Eqs. 9 and 11, is the mean bubble diameter. It should be noted that in obtaining the coefficient of the drag force and the corresponding bubble Reynolds number in model ω_S, not simply is the difference in the velocity of the phases used, like in model ω_G. Instead an instantaneous relative velocity $|\boldsymbol{v}_r|$ is used

$$|\boldsymbol{v}_r| = \sqrt{\boldsymbol{V}_r\cdot\boldsymbol{V}_r + 2(k_1 + k_2 - q_{12})} \tag{12}$$

which depends on its turn on the relative velocity between the phases $\boldsymbol{V}_r$ and is defined as

$$\boldsymbol{V}_r = [\,\boldsymbol{v}_2 - \boldsymbol{v}_1\,] - \boldsymbol{V}_d, \qquad \boldsymbol{V}_d = -\,\boldsymbol{D}_{12}^t\cdot\left[\frac{\Delta\alpha_2}{\alpha_2} - \frac{\Delta\alpha_1}{\alpha_1}\right] \tag{13}$$

Hence, an extra $\boldsymbol{V}_d$, the so-called drift velocity, is also taken in account. This drift velocity is a statistical quantity due to conditional averaging and may not be negligible. The drifting velocity accounts for the dispersion effects due to bubble transport by turbulent fluid motion. Its fluid-bubble dispersion tensor, denoted by $\boldsymbol{D}_{12}^t$ is written in terms of the fluid-bubble velocity covariance q_{12} and the fluid-bubble turbulent interaction time-scale τ_{12}^t. For practical computations, the dispersion tensor is restricted to its diagonal form

$$\boldsymbol{D}_{12}^t \equiv \frac{1}{3}\tau_{12}^t q_{12}\cdot\boldsymbol{I} \tag{14}$$

Where $\boldsymbol{I}$ is a 3×3 identity matrix. Noteworthy is that in model approach ω_G the same physical phenomena is modeled in the turbulent diffusion and can be treated as a turbulent drag term. Thus, model approach ω_S combines the drag and turbulent diffusion in a modified formula accounting for both effects.

The virtual mass force is the force exerted on a moving object when it accelerates relative to its surrounding. If an object immersed in a fluid is accelerated, it must accelerate some of the surrounding fluid. This results in an interaction force on the object. The formulation for both model approaches ω_G and ω_S are listed in Table 4 (Drew and Lahey 1987, 1990). The operator $D\cdot/Dt$ in model ω_G represents

Table 4. Two Different Sets for M_k, (k = 1,2)

Type of Force	Model ω_G	Model ω_S
Drag	$(-1)^{k+1}\alpha_2\,\rho_1 F_{D_G}(\boldsymbol{v}_2 - \boldsymbol{v}_1)$	$(-1)^{k+1}\alpha_2\,\rho_1 F_{D_S}\boldsymbol{V}_r$
Added Mass	$(-1)^{k+1}\alpha_2\,\rho_1 C_a\left(\frac{D\boldsymbol{v}_2}{Dt} - \frac{D\boldsymbol{v}_1}{Dt}\right)$	$(-1)^{k+1}\alpha_2\,\rho_1 C_a\left[\frac{\partial\boldsymbol{V}_r}{\partial t} + \boldsymbol{v}_2\cdot\nabla\boldsymbol{V}_r\right]$
Turb. Diff.	$(-1)^{k+1}\frac{\mu_1^t}{\alpha_1\alpha_2\sigma}F_{D_G}\nabla\alpha_2$	—
Fluc. Added Mass	—	$(-1)^{k+1}\nabla\left[\alpha_2\,\rho_1\left(\frac{2}{3}k_2 - \frac{1}{3}q_{12}\right)\right]$

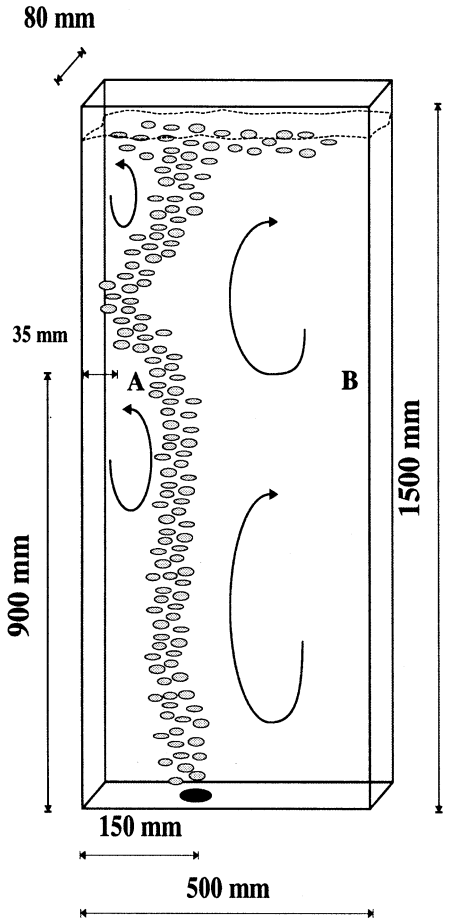

Figure 1. Geometry used for Becker experiment and CFD-simulations.

the material derivative

$$\frac{D\cdot_k}{Dt} = \frac{\partial \cdot_k}{\partial t} + \boldsymbol{v}_k \nabla \cdot_k \qquad (k = 1,2) \tag{15}$$

This particular form of the added mass force preserves Galilean invariance of the two-fluid model equations. The added mass force in model ω_S is more or less the same, but again the drift velocity V_d is taken into account. Like the drag force, the added mass force also contains a part due to fluctuating quantities, simply called the fluctuations on the added mass term. This term is only taken into account in model ω_S (see Table 4) and is linearly dependent on the turbulence intensity of the dispersed phase.

Benchmark Geometry

Experimental geometry and conditions

In order to test the capabilities of the models, the bubble plume experiment of Becker et al. (1994) is chosen for benchmarking. The geometrical setup, with all its dimensions, is shown in Figure 1. The sparger has a diameter of 40 mm and is located 150 mm from the left wall. The gas-flow rate in the experiment was put on 1.6-L/min.

Experimentally, it has been observed, using laser doppler anemometry (LDA) measurement techniques (Becker et al., 1994), that the plume starts to oscillate in a periodic fashion. The time series of the vertical liquid velocity in monitor point A shows oscillations with a more or less constant period of approximately 40 s. The amplitude varies between approximately $\pm$ 20 cm/s, and the average vertical liquid velocity is slightly negative, but differs not much from zero. The flow is in the turbulent regime, since the maximum Reynolds number based on the maximum velocity in monitor point A is 1.6×10^4, indicating that a turbulence model should be used.

Computational geometry and conditions

For the simulations, an in-house Finite Volume code ESTEEM (an acronym for Evolutionary Simulation of Turbulent Euler-Euler Multiphase flows), has been used. Storage of the flow variables is staggered and the code uses an implicit time-stepping algorithm and is pressure linked, based on the SIMPLE algorithm (Patankar, 1980; Lathouwers, 1999). All transport equations are solved by Krylov subspace iterative methods: CG for pressure and GMRES for momentum, gas fraction, and k-ϵ equations (see, for example, Saad and Schultz, 1986; Kaasschieter, 1988; Saad, 1997). A second-order Euler-backward scheme is used for the time-advancement (Ferziger and Peric, 2002), where the time derivative term is discretized as follows

$$\frac{\partial \Psi}{\partial t} = \frac{1}{2\Delta t}\left(3\Psi^{n+1} - 4\Psi^{n} + \Psi^{n-1}\right) \tag{16}$$

The spatial discretization is minimal second-order accurate; Total Variation Diminishing (TVD) schemes of third-order accuracy are used for convective transport and second-order central difference schemes are used for diffusive transport. All model constants used in the simulations are listed in Table 5.

For the simulations, a structured uniform computational mesh, with a grid density of $N_x * N_y * N_z = 38 * 52 * 18$ is used, combined with a constant time-step of $\Delta t = 0.05$ s. These choices are based on the study of Mudde and Simonin (1999). Two points have been chosen for monitoring the liquid velocity, that is, one at the location of monitor point A and the second is its mirror image with respect to the vertical center plane of the geometry (see Figure 1). The sparger is approximated by a square with approximately the same area as that of a circular one. The continuous phase is water and the dispersed phase is air. The gas bubbles are assumed to have a mean diameter of $d_b = 3$ mm. It should be noted that the slip velocity through all simulation was found to be approximately 20 cm/s. Since the volume fraction of the continuous phase α_1 is close to 1, the bubble-Reynolds number, as given by Eq. 11, is around 600. This justifies the use of Wen and Yu's correlation for rigid spheres. Physical inaccuracies are present in the drag coefficient model, since 3 mm bubbles can become ellipsoidal in reality.

Table 5. Model Constants Used for Two-Fluid and k-ϵ

C_μ	$C_{\epsilon,2}$	$C_{\epsilon,1}$	$C_{\epsilon,3}$	C_β	C_a	σ_{k_1}	σ_{ϵ_1}	σ_α	σ
0.09	1.44	1.92	1.2	0.45 or 1.80	0.5	1.0	1.3	1.0	1.0

Boundary conditions

For the present simulations, three distinct boundaries have to be considered, that is, the inlet, free surface, and walls. At the inlet, the gas volume fraction $\alpha_{2,\text{in}}$ is taken to be 0.0833 at a velocity of $v_{2,\text{in}} = 0.20$ m/s, while the liquid is at rest. The turbulent kinetic energy of the liquid is taken rather arbitrarily in the order of 10% $v_{2\text{in}}^2$ and set to 6.5×10^{-3} m^2/s^2, while the dissipation rate $\epsilon_1 = 1.1\times10^{-2}$ m^2/s^3.

At the free surface, the conditions for the continuous phase are the same as symmetry conditions in single-phase flow calculations. For the gas bubbles, other boundary conditions apply, namely

$$\frac{\partial v_2}{\partial n} = 0, \qquad \frac{\partial k_2}{\partial n} = \frac{\partial q_{12}}{\partial n} = 0 \tag{17}$$

Finally, the wall conditions are based on the so-called wall function approach of the k-ϵ model. The boundary layer at the wall is assumed to be in equilibrium for which a logarithmic velocity profile holds. As the dispersed phase wall friction is left out, the flow only notices the wall through the shear stress of the continuous phase. The liquid tangential velocity $v_{1,p}$ in the near wall region is obtained using the wall function for the liquid shear stress.

$$\tau_w = \frac{\rho_1 C_\mu \kappa \sqrt{k_{1,p}}}{\ln\left(E y_p^+\right)} v_{1,p}, \qquad y_p^+ = \frac{\rho_1 C_\mu^{1/4} \sqrt{k_{1,p}}}{\mu_1} y_p \tag{18}$$

Where the index p refers to a location to the near wall grid point and y_p^+ is the dimensionless wall distance. The parameter κ is the Von Karman constant and equals 0.41, while E specifies the roughness of the wall (set to 8.432 for a smooth wall).

Results and Discussion

Model benchmarking

All simulations on the chosen grid and time-step size were performed on a Pentium III 800 MHz PC with a single processor running under Linux. Typical runs for simulating 300 s real time took about 2 days. Both model sets due to Gosman et al. and due to Simonin et al. were used in the simulations. At first, the models were tested as bold as possible, that is, only the drag force was taken into account and the extra terms in the k-ϵ were neglected. Then, in the following runs, the effect of two-way coupling and effects of turbulent diffusive forces, as well as the added mass force, were taken into account. For all computations unless mentioned otherwise, the so-called ISNAS limiter (Zijlema, 1996b) was used in the TVD scheme.

Approach of Gosman et al.: model M (ψ_G, ω_G).

In the first set of simulations the model approach due to Gosman is used. Just a couple of seconds after the bubble injection is started, the plume reaches the free surface and then moves towards the wall. In this startup phase of the simulation (that is, approximately the first 80 s) the formation of circulation cells are observed in the upper lefthand corner of the geometry at the boundary of the plume. These circulation cells were observed both in the experiments of Becker et al. (1994) and Mudde et al. (1997). One clearly observes from Figure 2 that the oscillation in two monitor points are in anti-phase, having a period of approximately 30 s. The oscillations in the monitored vertical liquid velocity is caused by vortices moving from the top, starting at the free surface, to the bottom in an alternating way.

The same simulation was conducted again, but also now the influence of the bubbles was taken into account, that is, the extra source-terms in the k-ϵ turbulence model was included (so-called two-way coupling). The vertical liquid velocity in monitor point A as a function of time is shown in Figure 3. When inspecting Figure 3, two different alternating waves can be distinguished, one having a somewhat larger amplitude than the other. The inclusion of two-way coupling on turbulence strengthens this phenomenon. This means that the vortices, which move from top to bottom, differ in strength.

When turbulent diffusion is also included, several new phenomena are observed (see Figure 4). The strength of the

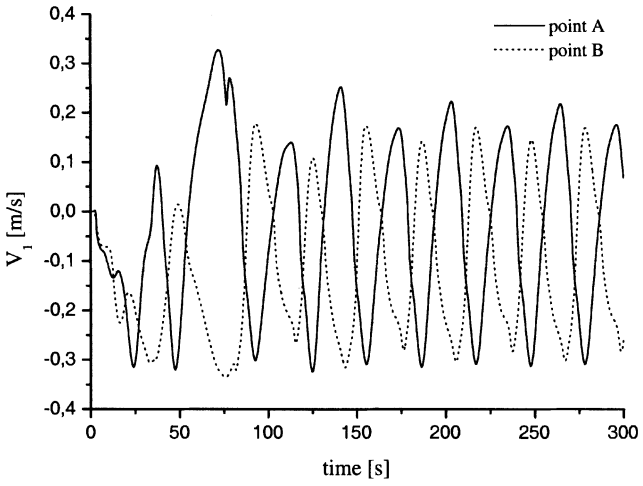

Figure 2. Vertical velocity in monitor points: Gosman's model approach with drag only.

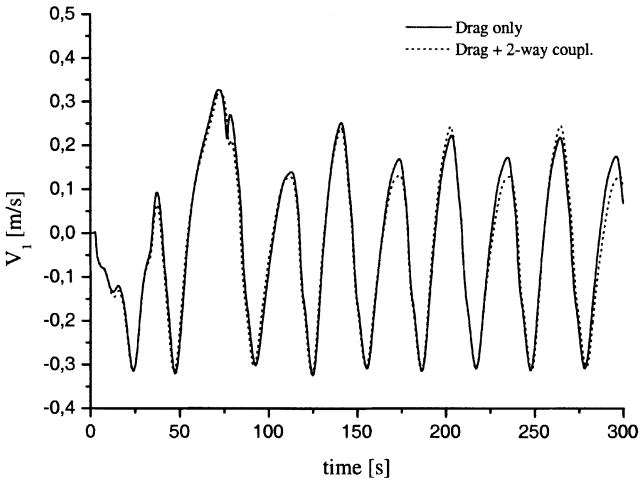

Figure 3. Effect of two-way coupling in Gosman's model approach: vertical velocity in monitor point A.

weak vortex is weakened more, while its period is slightly increased. The stronger vortex on the other hand gains in strength and moves significantly slower from top to bottom, resulting in a longer period in the monitored liquid velocity. Another striking difference is that the plume is now more smeared out in the higher region, near the free surface. Also, lower peak values are found when examining the gas fraction profile along the bubble plume.

At the final stage, added mass is also taken into account. This force is important when acceleration effects play a role such as in the vicinity of the inlet. From Figure 5, it can be seen that the added mass force has a minor effect on the overall dynamics of the plume. The vortical strength and period changes are negligibly small in the first 250 s of the simulation. When extending the runs several hundred seconds more, only minor changes can be observed.

From the full Gosman's model approach, eight snapshots of the mid-crossectional liquid velocity field and the gas fraction profile are presented in Figure 6 in the time-interval $t =$ 160 s up to $t = 230$ s. The time-difference between subsequent frames is constant and equals 10 s. When observing Figure 5, the presented time-interval shows the flow situation in one "cycle." The mean period of the oscillations are approximately 35 s, with an amplitude of 20 cm/s for the vertical component of the liquid velocity in monitor point A, while the time-averaged vertical liquid velocity is slightly directed downward. When observing the snapshots of Figure 6, a vortex is created in the righthand upper corner, at time $t = 170$ s. Also, a vortex cell is present at the lefthand side of the plume, at the free surface. Observe from Figure 5 that these vortices represent the "weak pair." Both vortices gain in strength with time. When the righthand side vortex reaches a critical size, it starts to move downwards ($t = 180$ s). During this movement, the vortex splits in two parts due to the vortex on the lefthand side of the plume, where one part stays in the upper righthand side corner ($t = 190$ s). A half oscillation period later, the lefthand side vortex has reached its critical size and moves downward (note that the vortex core on the lefthand side vortex is more or less located at the plume interface). In a half oscillation period, the vortex which stayed in the upper righthand side corner has enough time to grow bigger in size than the former righthand side vortex (see $t =$ 200 s). Unlike the former righthand side vortex, it moves as a whole downward when it has reached a critical size (see $t =$ 210-s). In the lefthand side corner, a vortex cell is again created at the free surface. This upper lefthand side vortex has again approximately half an oscillation period to grow, but will gain more strength than the former lefthand side vortex, since there is no vortex on its righthand side to prevent this. Due to its increased strength, the lefthand side vortex has now the ability to reach the bottom of the geometry, while the former lefthand side vortex died out before it could reach the bottom. At this point, the "cycle" is repeated again.

Approach of Simonin et al.; model M (ψ_S, ω_S)

The same test cases were done in the same order using the model approach of Simonin et al. At first, the drag force was considered to be the only interfacial force. Note that, as already mentioned earlier, the turbulent diffusive force is incorporated in the drag force model. Like in Gosman's model approach, the startup phase of the simulation is approximately 80 s. The formation of circulation cells are observed in the upper lefthand side corner, in the vicinity of the plume, at the free surface. The simulation again reveals that vortices move from the top, at the free surface, to the bottom in an alternating way. In Figure 7 the simulations with drag only for both models are shown. What would intuitively be expected is that the differences would be more or less the same as the differences, as shown in Figure 4, that is, the differences generated by turbulent diffusion. However, the turbulent diffusive force in Simonin's model approach has minor influence in the first 200-s, while, in Gosman's model approach, a significant effect starts to show up approximately after the startup phase. Also, in Simonin's model approach the effect after 200 s is different: the amplitudes of the waves are slightly decreased, making the two types of wave phenomena disappear. Also, the period is decreased in contrast to what was found using Gosman's model approach, which showed a slight period stretching. The differences can be un-

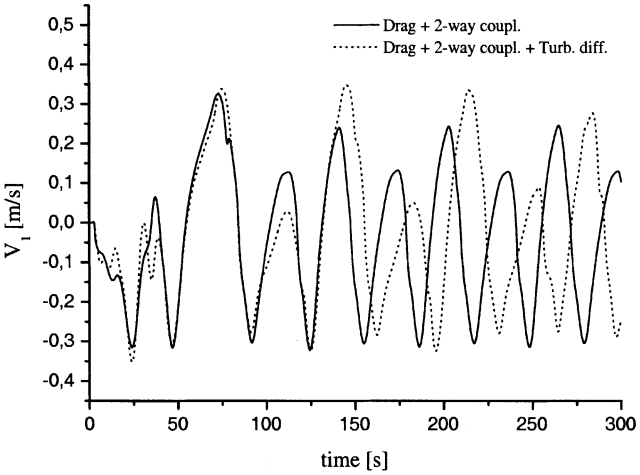

Figure 4. Effect of turbulent diffusion in Gosman's model approach: vertical velocity in monitor point A.

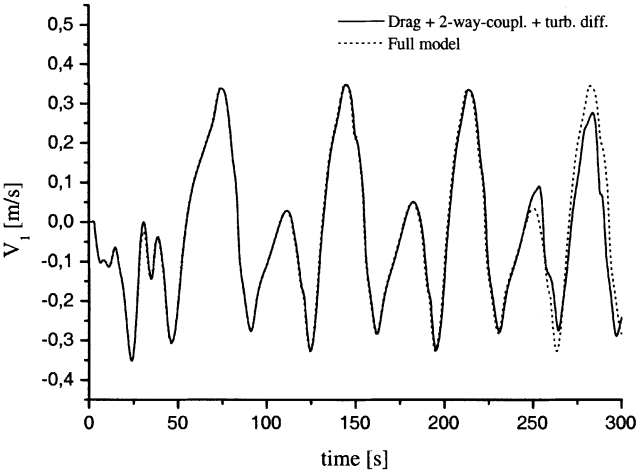

Figure 5. Effect of added mass in Gosman's model approach: vertical velocity in monitor point A.

derstood, since, in Gosman's model approach, the turbulent diffusive force is linearly superposed on the drag force, while in Simonin's model approach, the drift velocity, which plays a major part in describing this force, is also incorporated via the Reynolds number in the drag force coefficient (see Eqs. 9 and 11). Separate studies (not shown here) have revealed that changing the drag coefficient has a large influence on the vortex strength and speed.

In the second stage, the extra source terms in the k-ϵ equations are taken into account, the differences are minor like in the Gosman's model approach (see Figure 8). When the added mass force is taken into account, it shows to have more influence on the oscillation pattern than the added mass force in case of the Gosman's model approach. Figure 9 shows that, in the long run, the added mass force increases the period, while not affecting the amplitude of the oscillation. This is due to the fact that the added mass force is also a function of the so-called drift velocity. In spite of its significant influence, the simulations reveal, like in the former model approach, that the added mass force is still at the largest an order of magnitude smaller than the governing drag force. The added mass force is quantitatively largest in the vicinity of the inlet, that is, where the acceleration rates are highest and become smaller in magnitude from bottom to top.

Finally, the fluctuating part of the added mass is included (see Figure 10). This part, which can be interpreted as the added mass of the bubbles due to the fluctuating liquid-velocity field, shows to have an opposite effect as the addition of added mass force in the first 150 s of the simulation. In the second part of the simulation the fluctuating part of the added mass influences the amplitude of the oscillation and, thus, the strength of the vortices.

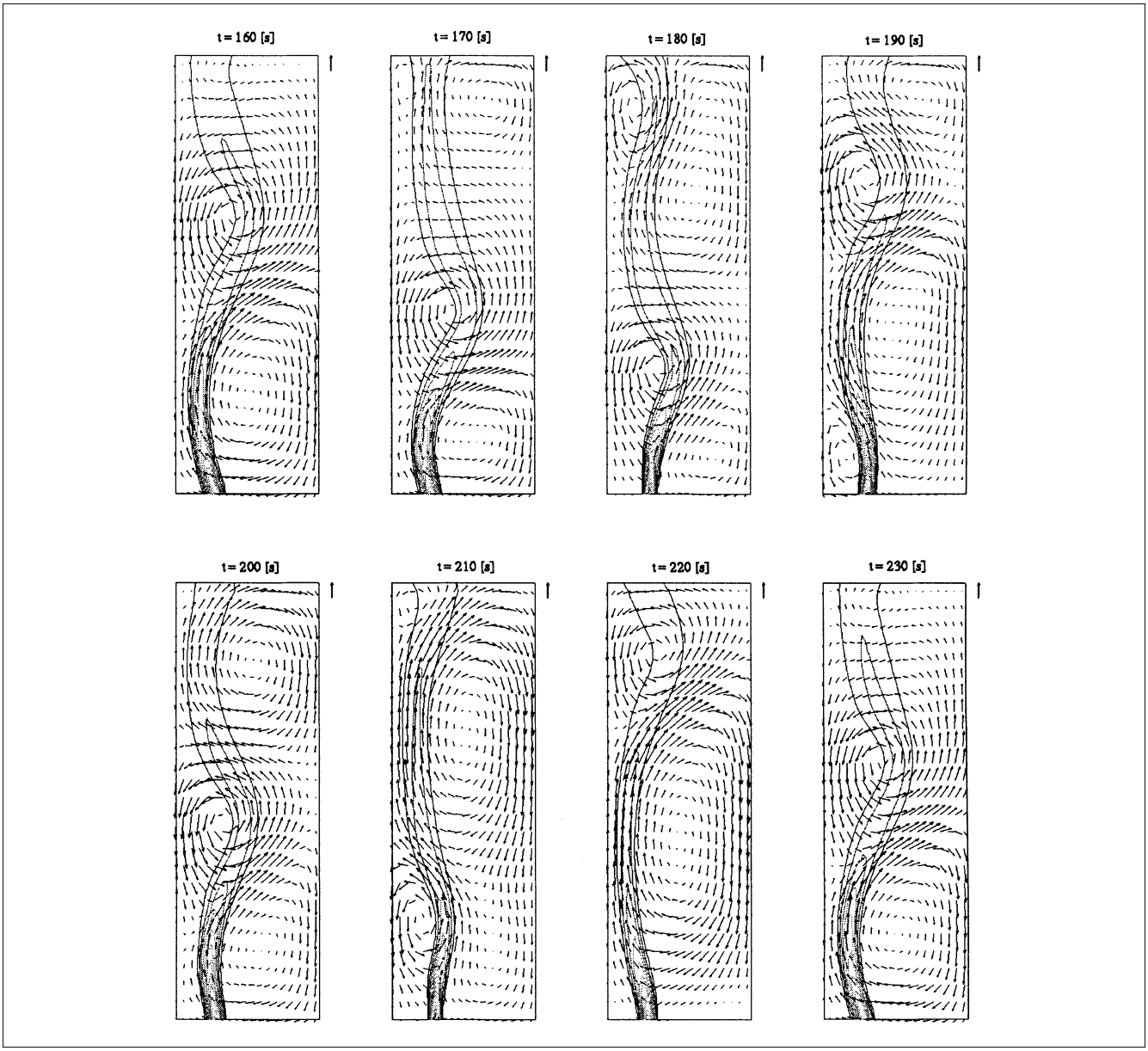

Figure 6. Snapshots of the bubble plume, with Gosman's model approach between $t = [160, 230]$s: magnitude of reference vector is 20 [cm/s].

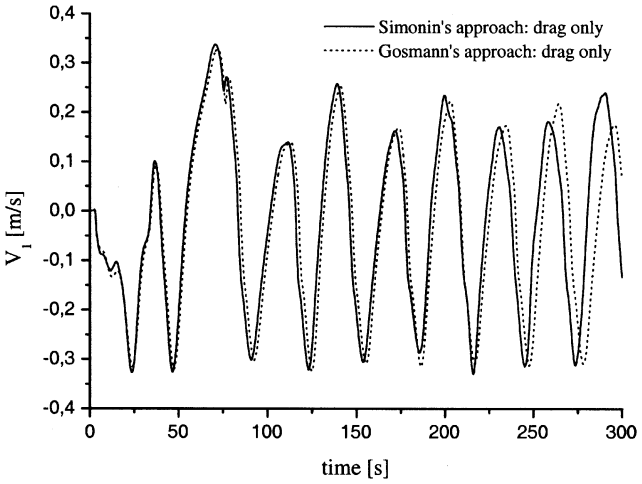

Figure 7. Comparison of Simonin's model with that of Gosman's approach considering drag as the only interfacial force.

Snapshots on the same time interval $t = [160, 230]$ s are shown in Figure 11, with a time-difference of 10 s between subsequent frames. Although the oscillations in the monitored liquid velocity seem to be more irregular than in the case using Gosman's model, not many differences can be observed regarding the liquid velocity field and gas fraction profile. The irregularity stems from the fact that the vortex breakup process, discussed in the former section, is more irregular than in the case of Gosman's model approach. For example, observe the snapshot at time $t = 210$ s. The upper righthand corner vortex, which is about to move downwards, will still leave a small part behind (see $t = 220$ s). This is contrary to when the Gosman model approach is used (see Figure 6). The mean period of the oscillations, which is approximately 33 s, is somewhat smaller than in the case of Gosman's model. However, the amplitude of the liquid velocity is still in the order of 20 cm/s and has a slight negative time-averaged value at the location of monitor point A.

It should be noted that experiments (Becker et al., 1994) showed that the plume stays almost attached to the lefthand side wall at approximately one-third of its length, while the simulations with both models revealed a slight movement of the plume in this region. Experiments show that the tendency of the plume to stay attached to the wall depends on the gas-flow rate. In this case the shear rate near the inlet will increase, and this plays a role in the lift force. This could possibly push the plume towards the lefthand side wall in the vicinity of the inlet. However, in the present simulations the lift force is excluded.

At this stage, several things can already be concluded. From the interfacial forces, which can be decomposed in a mean and fluctuating part, the drag force shows to be the force with the largest impact. The fluctuating part of the forces showed to have a dispersive effect on the plume dynamics. The (mean) drag force is sufficient to capture the oscillating behavior of the plume, while the (mean) added mass plays a minor role in the plume dynamics. This will be become clearer when, for instance, Gosman's model approach is considered for estimating the magnitude-ratio in the mainstream direction of (mean) added mass force to the (mean) drag force (see Figure 12). Observe that the added mass force is of the same order of magnitude as the drag force, in the vicinity of the inlet. Delnoij et al. (1997) stated that the added mass force becomes significant at this particular location. Note also that, for the given time frames ($t = 180$ s and $t = 190$ s), Figure 12 shows spots of relatively high added mass force, where the left wall vortices in Figure 6 are located. This was to be expected, since, at vortices, centrifugal forces occur, inducing acceleration rates. The added mass becomes more insignificant towards the free surface. In the substream direction the drag force becomes much smaller and the force ratio becomes several orders higher. In these directions the added mass has a significant stabilizing role.

Previous findings about the added mass force are in contrast to the findings of Mudde and Simonin (1999). Their nu-

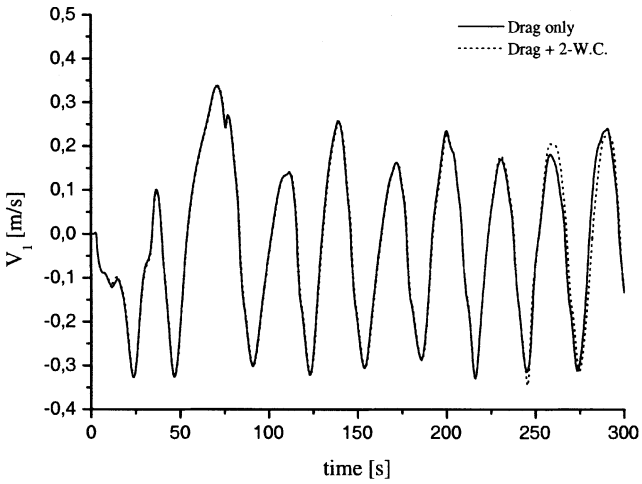

Figure 8. Effect of two-way coupling in Simonin's model approach. vertical velocity in monitor point A.

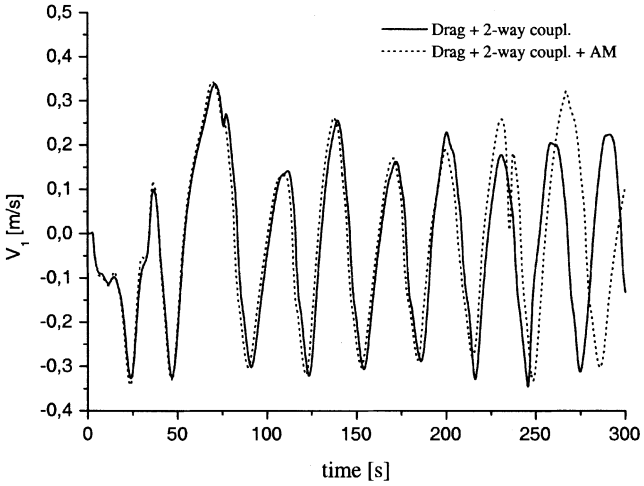

Figure 9. Effect of added mass in Simonin's model approach: vertical velocity in monitor point A.

merical simulation, using ASTRID version 3.3 when just drag is considered as interfacial force, generated a plume which stays attached to the wall. The plume only showed some perturbed motion near the free surface. Mudde and Simonin found that the plume starts to oscillate when the added mass force was also accounted for. To find out what causes these differences, the simulations were conducted again, using a newer version (version 3.4) of the ASTRID-code, but still using the same model equations. The obtained results are in line with the presented results: drag as the only interfacial force seems to be sufficient to bring the plume in an oscillating state. When taking the added mass force into account, in the ASTRID-code (which equals turning on the mean and fluctuating part of the added mass) the effect showed to be more or less the same as in the presented simulations. It is unfortunately unclear why the results found by Mudde and Simonin showed no oscillation when just drag is considered as the interfacial force.

The presented results bring so far the results of both codes, ESTEEM and ASTRID, in line with the findings of Sokolichin and Eigenberger (1999). They have considered drag as the only interfacial force in their drift-flux model approach and observed an oscillating bubble plume, having a similar amplitude and period as found in the presented simulations.

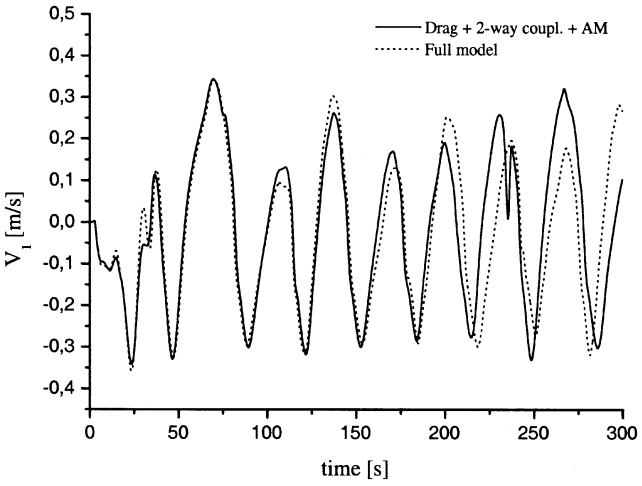

Figure 10. Effect of added mass fluctuations in Simonin's model approach: vertical velocity in monitor point A.

Convective transport

TVD Approach; Choice of Limiters. The straightforward replacement of the first-order upwind space discretization for convective transport by appropriate second-order accurate formulas leads to deficiencies similar to those encountered with central schemes, namely the generation of oscillations around discontinuities. Harten (1983) introduced the concept of Total Variation Bounding (TVB) of the solution, which is a more general concept of Total Variation Diminishing (TVD). The idea is to ensure that unwanted oscillations, which make convergence problematic, are not generated by a numerical scheme. Another requirement of the scheme is that the converged solution should also be physically acceptable and fulfill certain entropy conditions.

General families of schemes satisfying the mentioned requirements can be defined (Harten, 1983; Hussaini et al., 1997), but it is shown that these schemes can only be first-order accurate. To overcome this limitation, a certain nonlinear reconstruction technique is needed for the convective fluxes. This important concept was introduced initially by Van Leer (1973, 1974) under the form of so-called "flux-limiters," which control the gradients of the computed solution such as to prevent the appearance of over- or under-shoot. Consider the following 1-D scalar convection equation

$$\frac{\partial \Psi}{\partial t} + \frac{\partial U\Psi}{\partial x} = 0 \tag{19}$$

where U is a given convective velocity, and Ψ the scalar to be determined. When discretizing Eq. 19 in a space combined with an implicit time-stepping scheme, the following equation is obtained

$$\Psi_i^{n+1} = \Psi_i^n - \frac{\Delta t}{\Delta x}\left[(U\Psi)_{i+1/2}^{n+1} - (U\Psi)_{i-1/2}^{n+1}\right] \tag{20}$$

where Δt and Δx are the time step and the mesh width, respectively. For example, the convective flux through the right face of the control volume (see Figure 13) is given by

$$\Psi_{i+1/2} = \begin{cases} \Psi_i + \frac{1}{2}\phi\left(r_{i+1/2}^{+}\right)\left[\Psi_{i+1} - \Psi_i\right] & \forall U_{i+1/2} \geq 0 \\ \Psi_{i+1} + \frac{1}{2}\phi\left(r_{i+1/2}^{-}\right)\left[\Psi_{i+2} - \Psi_{i+1}\right] & \forall U_{i+1/2} < 0 \end{cases} \tag{21}$$

$$r_{i+1/2}^{+} = \frac{\Psi_{i+1} - \Psi_i}{\Psi_i - \Psi_{i-1}}, \qquad r_{i+1/2}^{-} = \frac{\Psi_{i+1} - \Psi_i}{\Psi_{i+2} - \Psi_{i+1}} \tag{22}$$

By introducing the so-called "flux-limiting function" ϕ, which is made a function of the local and upwind gradients of the solution (see Eq. 22), the discretization scheme given by Eqs. 20 and 21 can be made higher-order accurate, while still being TVD. Note that when the flux-limiter ϕ is set to zero, the first-order upwind scheme is recovered.

Despite that most "flux-limiters" make the scheme globally second-order accurate and have substantial merits, they have one major defect. The schemes are not able to distinguish between a shock profile or a smooth extremum, and the accuracy of the scheme will, therefore, locally degrade to first-order accuracy. In the latter case, the amount of numerical diffusion which will be added to stabilize the scheme will be in generally too much. The profile will be smoothened more and leads to a less sharp profile than the actual solution should give. In our bubbly flows simulation this situation can occur frequently at the interface of the bubble plume: the volume fraction profile will be smeared out more than the exact solution would be. Since the flow is time-dependent, this local accuracy degeneration contaminates the whole flow

field in the long run. To solve this problem, the limiter is modified into a uniformly accurate one (Hussaini et al., 1997; Zijlema, 1996a), that is, "flux-limiter" preserves second-order accuracy near extrema and sharp gradients.

All simulation in the former two section were performed with the third-order, uniformly accurate ISNAS limiter $\phi(r)$ (Zijlema, 1996b). This limiter is a linear combination of the third-order accurate ISNAS limiter $\phi^+(r)$ and the limiter $\phi^-(r)$ (see Table 6). The latter is switched on near extrema and sharp gradients, while the first is switched off to preserve higher-order accuracy.

A comparison is needed to test the accuracy and the effect, the change of limiter has on the flow field and the dynamics of the bubble plume. Therefore, both full model simulations were repeated using the second-order accurate Van Leer limiter and the more diffusive second-order MinMod limiter (see Table 6). Both limiters degrade the spatial discretization scheme to first-order accuracy near extrema and sharp gradients. The results with the different limiters for Gosman's model approach are shown in Figure 14. One observes that the Gosman's approach, combined with the Van Leer limiter shows not much difference with the original simulation. However, in the long run the differences become larger. The simulations with the MinMod limiter are shown to have large differences with the original and the Van Leer limiter. There is again a shift in the oscillations, larger than in the case of

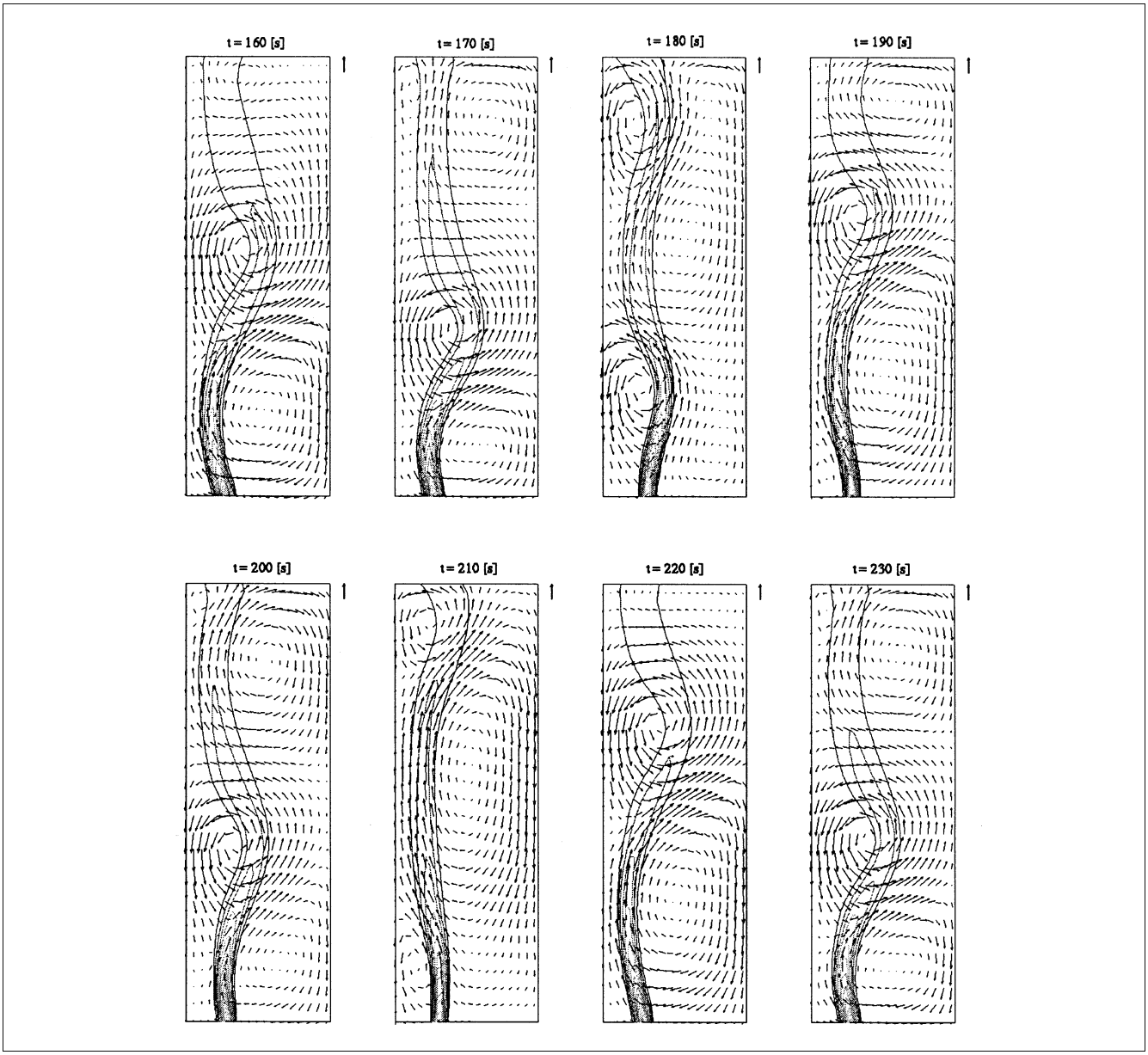

Figure 11. Snapshots of the bubble plume, with Simonin's model approach between $t = [160, 230]$ s.

Magnitude of reference vector is 20 [cm/s].

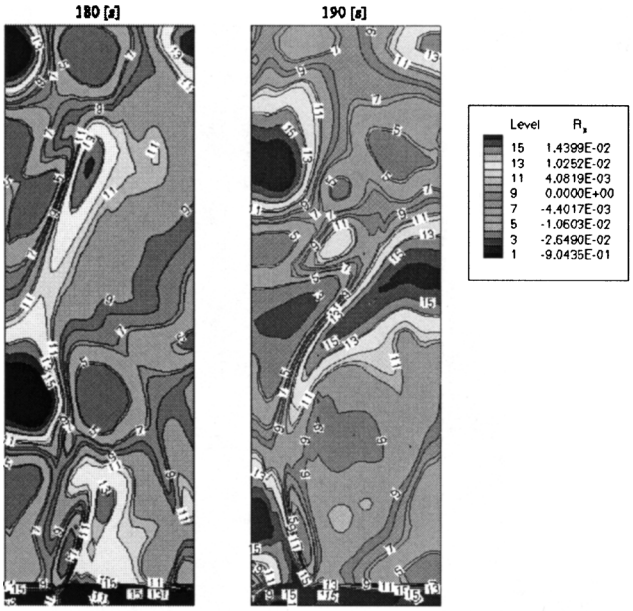

Figure 12. (Added mass/drag)-ratio in the main-stream direction for the full Gosman's model approach on times $t = 180$ s and $t = 190$ s.

the Van Leer Limiter. However, a striking difference is that now the stronger vortex is decreased in strength and the weaker vortex increased in strength.

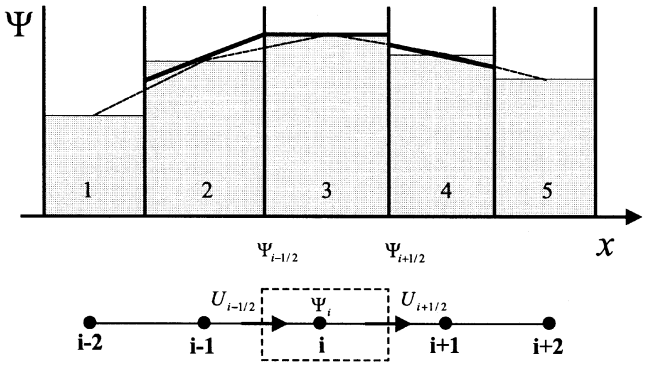

Figure 13. Representation of flux reconstruction process:

The heavy lines denoted reconstructed gradients. In cell No. 3 no gradient is allowed since this will accentuate the existing maximum. At cell No. 4, unlike cell No. 2, no restriction is applied since the gradients are almost the same.

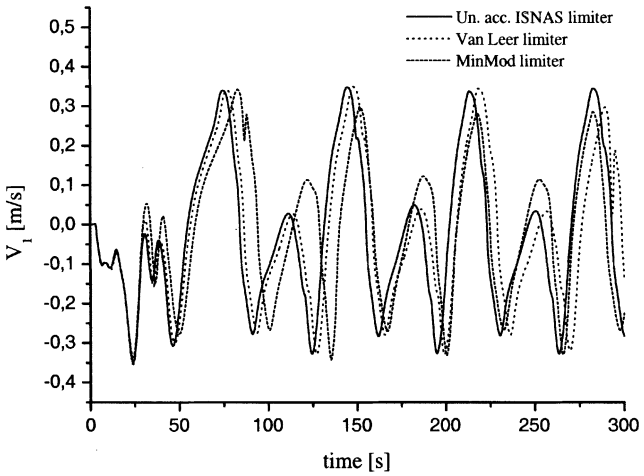

Figure 14. Gosman's full model approach: the effect of different limiters.

The same numerical experiment was performed for the full model approach due to Simonin et al. using the Van Leer and MinMod limiter. Figure 15 shows the effect of the limiter on the original simulations. When using the Van Leer Limiter, the differences are minor and only show a slight shift in the oscillation. Again, in the long run, these differences

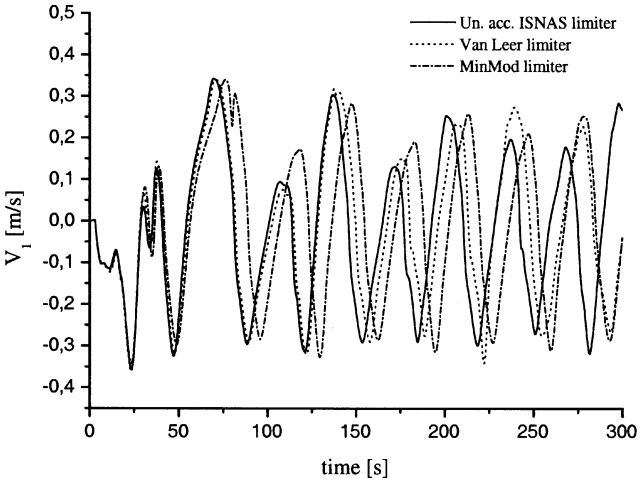

Figure 15. Simonin's full model approach: the effect of different limiters.

Table 6. Three Limiters Used in TVD Schemes

	Limiter Type	
	U.A. ISNAS	$\phi(r) = \frac{1}{2}[1+\text{sign}(r)]\phi^+(r) + \frac{1}{2}[1-\text{sign}(r)]\sigma^-(r)$
		$\phi^+(r) = \frac{1}{2}\frac{(r+\lvert r\rvert)(r+3)}{(1+r)^2}$ $\quad \phi^-(r) = \min\left[0, \max\left(-\frac{1}{8}, \frac{1}{8}r\right)\right]$
	Van Leer	$\phi(r) = (r+\lvert r\rvert)/(1+r)$
	MinMod	$\phi(r) = \max[0, \min(r,1)]$

become larger. The MinMod limiter generates differences with the original simulation, which are overall larger than the simulations performed using the Van Leer limiter.

The results show numerical errors, which are introduced in the convection schemes, by a nonproper choice of the flux-limiting function. These errors cause significant differences in the solution compared to the accurate solution. The differences are of the same order of magnitude as certain physical phenomenon (change of vortex strength and speed) that specific interfacial forces can introduce (such as turbulent diffusion and added mass).

Upwind discretization; $\phi = 0$

In the previous section some numerical experiments were done with limiters. To some extent the diffusion can be varied by using more diffusive limiters. Differences in the behavior of the plume dynamics are observed. At this stage, two questions arise: at first, is there a critical amount of numerical diffusion that can be added to the discretized balance equations to obtain a static plume. Secondly, which equation of the model governs the dynamics of the plume. To answer these questions, it is sufficient to consider the full model approach of Gosman. Again, the simulations have been performed, using the uniformly accurate ISNAS limiter. The difference now is that, partially, the convection schemes in the mass, momentum, and turbulence equations are changed into first-order upwind schemes, that is, the flux limiter ϕ is set to zero.

Four identical cases were performed, with the difference that, in the first case, first-order upwind was used for convective discretization in the dispersed phase mass balance equation and the original TVD schemes for the rest of the equations. In the second case, upwind is used for the dispersed phase momentum equation only. In the third case, upwind is used for the continuous phase momentum equation, while, in the final case, first-order up winding is used for convective transport for the turbulence equations. Figure 16 shows the vertical velocity in monitor point A as function of time.

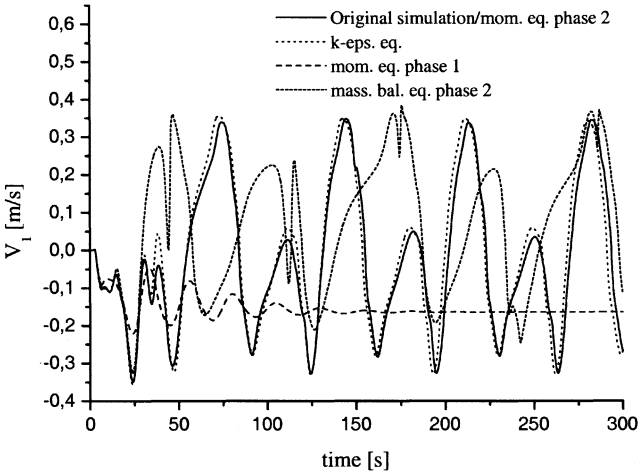

Figure 16. Plume dynamic behavior due to excessive numerical diffusion in Gosman's model approach.

Using upwind for the dispersed mass balance equation (this is the equation used to determine the gas volume fraction) has a tremendous influence on the plume dynamics. The two types of waves are still observed, but the period is increased significantly. The periods of the waves are approximately doubled, while the time-averaged velocity is shifted upward. When observing the void fraction profile at a time-instant (see Figure 17), a clear smearing and decreased peak-values of the gas volume fraction is observed. This is caused by the excessive amount of numerical diffusion due to first-order up winding in the dispersed mass balance equation. Note also that the core of the left vortex has more or less moved towards the center of the plume, as observed in the accurate solution.

When upwind is used for the dispersed phase momentum equations only, the vertical velocity at the monitor point resembles the original simulations with a full TVD convective discretization. Probably, the momentum of the dispersed phase does not determine and influence the bubble plume oscillation at all. This justifies the use of a drift-flux model, as done by Sokolichin and Eigenberger (1999). However, when first-order upwind is used for convective transport in the continuous-phase momentum equation, the velocity in the monitor point resembles a critical dampened oscillator (see Figure 16). The plume will oscillate due to the fact that the circulation cell, which is formed in the upper lefthand side corner, starts to grow and moves downward. Halfway, the vortex is captured by the plume and the left wall. This vortex will oscillate at a certain height, near the monitor point until the total flow field obtains a steady-state character. The vortex is then frozen at a certain height. Sokolichin and Eigenberger (1999) also obtained a steady-state plume, which stays more or less attached towards the lefthand side wall when using first-order upwind schemes in their drift-flux simulations. The steady-state situation is shown in Figure 18.

Only small differences are observed when first-order upwinding is used for convective transport in the k-ϵ model. This is in line with the expectation that in a k-ϵ model, which is based on the local equilibrium assumption, the process is governed by the production and dissipation of turbulence. The addition of a small amount of numerical diffusion to the much larger turbulence model diffusion has minor effect on the total turbulent kinetic energy k and turbulence dissipation ϵ. Similar observations were made by Sokolichin and Eigenberger (1999), in their drift-flux approach. They observed no significant changes when using first-order upwind for convective transport in the k-ϵ model.

Time step and grid dependency

It is well known that convergence behavior of CFD simulations can deteriorate when the time-step size is chosen too large and does not fulfill the so-called CFL condition (Hirsch, 1990

$$\lambda_{\max} \frac{\Delta t}{\Delta x} \leq 1 \tag{23}$$

Δt and Δx represent the time-step size and mesh width, respectively. $\lambda_{\max}$ is the largest eigenvalue of the discretized system of equation to be solved. Equation 23 states physically that a wave (or a package of information) is allowed to travel,

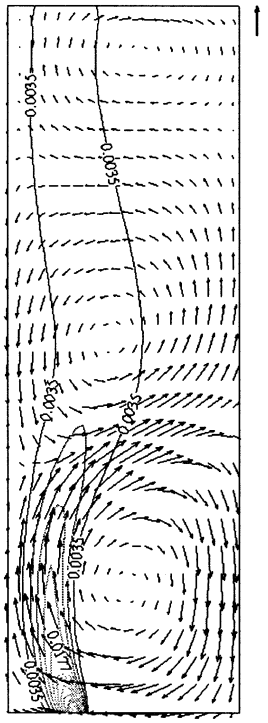

Figure 17. Gas-fraction profile smearing due to first-order upwind in the dispersed phase mass balance equation.

Reference vector = 20 cm/s.

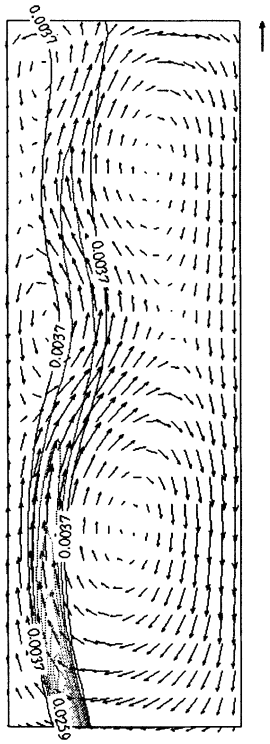

Figure 18. Steady-state solution obtained due to first-order upwind in continuous phase momentum equation.

Reference vector = 20 cm/s.

at most, one cell unit. This condition is more strict when using explicit time schemes. For implicit-time schemes, which are applied in the present study, the conditions are less strict. Still, the time-step size cannot be taken too large, since the numerical diffusion will increase and degrade the accuracy. As was said before, the time-step size $\Delta t = 0.05$ s was chosen based on the findings of Mudde and Simonin (1999). In this section it will be shown that for the performed simulations the chosen time-step size was indeed small enough. Two additional simulations, identical to the original simulations using the full Gosman's model approach, were performed with different time-step sizes, namely $\Delta t = 0.1$ s and $\Delta t = 0.025$ s. The oscillation trend of the velocity in monitor point A is depicted in Figure 19. The results show clearly that a time-step of $\Delta t = 0.1$ s is too large, making the plume oscillations diverge from the two simulations, leading to large differences in the prediction of the mean amplitudes and frequency. The simulation performed with the smallest time-step shows a slight shift of the period. This shift stays more or less constant when pursuing the simulation run over a longer time than 300 s.

As already mentioned in the introduction, the accuracy can be improved by grid refinement. However, 3-D computations are very costly and one prefers to do the computation at a grid which is as coarse as possible, but still giving a good picture of the overall dynamics. To check if the chosen base grid fulfilled the conditions, the simulation with the full Gosman's model approach was conducted again with a grid doubling in each direction. The results are shown in Figure 20. This figure indicates that the startup phase is reduced and the plume is set in motion earlier than in the base-grid simulations. This is expected since less numerical diffusion is added to the system enhancing instability. Still, the two type of wave phenomena is observed, with just minor changes in the amplitudes, while the periods are preserved and no smaller structures are created. The base-grid is, therefore, sufficient to capture the overall dynamics well.

Conclusions and Recommendations

A transient bubbly flow has been analyzed and modeled by the Two-Fluid formulation, combined with a, for two-phase flow modified, k-ϵ turbulence model. The models are implemented and solved by an in-house code ESTEEM. The sensitivity of the model and code performance with respect to numerical diffusion were investigated. Two different model approaches, regarding the interfacial closure in the Two-Fluid formulation are tested. The first is due to Gosman and coworkers and the second is due to Simonin et al. As a benchmark, the so-called "Becker experiment of a meandering plume" was used. The simulations show that for the chosen benchmark, the models do not exhibit much differences in the global dynamics. The predicted oscillation period and amplitude are more or less the same, and compare fairly good with experimental observations. However, Gosman's model approach shows more regularity in the dynamics (the vortex breakup process), which is not known if this is experimentally observed.

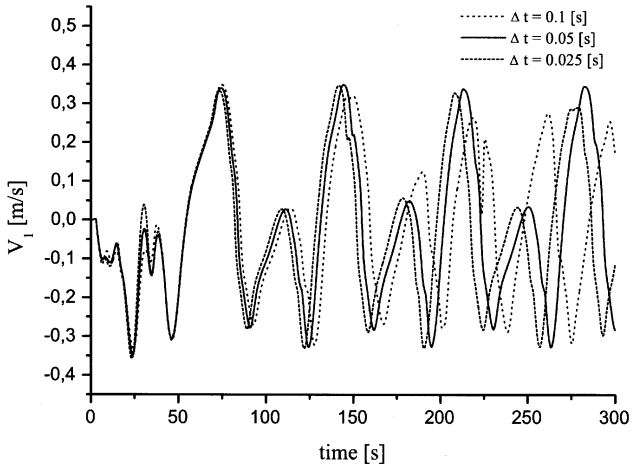

Figure 19. Dependency of the solution on time-step size.

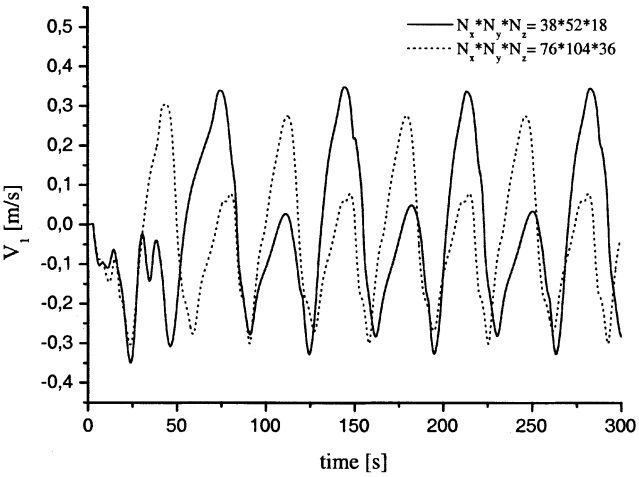

Figure 20. Dependency of the solution on grid-size.

The drag force was in both cases sufficient to capture the global dynamics of the bubble plume. The effect of the interfaces on the turbulence (so-called two-way coupling), the turbulent diffusion force, the added mass force and its fluctuating part have a more or less "tuning effect." The bubbly flow shows to be quite sensitive for numerical errors acting like artificial diffusion. It was shown that by using more diffusive limiters (Van Leer and MinMod) in the TVD scheme leads to errors with the same order of magnitude as the earlier mentioned tuning effect caused by the interfacial forces. When the limiter is set to zero in the TVD scheme, that is, using first-order upwind for convective transport, a "limit" was found for the numerical diffusion to be added that causes a steady-state situation. The effect of using first-order upwind for convective transport is studied by partially setting the limiter to zero in the transport equations for mass, momentum for each phase, and turbulence. The results show that an excessive amount of numerical diffusion in the momentum balance for the continuous phase kills the transient character of the flow. When using first-order upwind in the dispersed phase mass balance equation, the flow stays transient but the character of the oscillation changes drastically. A minor or no effect was observed when a large amount of numerical diffusion was introduced in the k-ϵ equations and dispersed-phase momentum balance, respectively.

As mentioned earlier, the pressure forces and their effects are not discussed here. This should be done in a subsequent study. Also, the lift force was not accounted for in this study. However, this force can still become significant, especially at the passage of a vortex. The following order of magnitude analysis shows this when, for example, the transversal component (width-direction) of the potential lift force model

$$F_L = C_L \rho_1 \alpha_2 (\boldsymbol{v}_1 - \boldsymbol{v}_2) \times (\nabla \times \boldsymbol{v}_1) \tag{24}$$

is compared in magnitude against the corresponding transversal component of the drag force, as described in Gosman's model approach. Then, the following ratio is obtained

$$\frac{F_{L,w}}{F_{D,w}} = \frac{4}{3}\frac{C_L}{C_D} d_p \times \frac{(v_1 - v_2)\left(\frac{dv_1}{dx} - \frac{du_1}{dy}\right) + \overbrace{(w_1 - w_2)\left(\frac{du_1}{dz} - \frac{dw_1}{dx}\right)}^{\approx 0}}{(u_1 - u_2)\underbrace{\sqrt{(u_1 - u_2)^2 + (v_1 - v_2)^2 + (w_1 - w_2)^2}}_{\approx (v_1 - v_2)}} \approx \frac{4}{3}\frac{C_L}{C_D} d_p \frac{\omega_{xy}}{(u_1 - u_2)} \tag{25}$$

From a rough estimation of the simulation results, it follows that when a vortex is passing the bubble plume, the following values in the vicinity of the plume are found: vorticity strength $\omega_{xy} = 6_s^{-1}$ and slip velocity in transversal direction $(u_1 - u_2) \approx 1.5$ cm/s. With $C_L = 0.5$, $C_L/C_D \approx 1$, $d_p = 3$ mm, one observes that the lift force component in the transversal direction has the same order of magnitude as the corresponding drag force component. Therefore, further research where the effect of this force is studied in detail is needed.

Acknowledgment

The support is gratefully acknowledged of Prof. Simonin of the Institute de Mechanique des Fluides de Toulouse (IMFT), who gave us the possibility of performing some numerical simulations with the ASTRID-code and doing some code-comparison.

Literature Cited

Auton, T. R., "The Lift Force on a Spherical Body in Rotational Flow," *J. Fluid Mech.*, **183**, 199 (1987).

Becker, S., A. Sokolichin, and G. Eigenberger, "Gas-Liquid Flow in Bubble Columns and Loop Reactors: II. Comparison of Detailed Experiments and Flow Simulations," *Chem. Eng. Sci.*, **49**, 5747 (1994).

Bel F'dhila, R., and O. Simonin, "Eulerian Predictions of a Turbulent Bubbly Flow Downstream a Sudden Pipe Expansion," *Sixth Workshop on Two-Phase Flow Predictions*, Erlangen, Germany, M. Sommerfeld, ed., 264 (1992).

Bunner, B., and G. Tryggvason, "Direct Numerical Simulations of

Dispersed Flows," *Proc. of the 9th Workshop on Two-Phase Flow Predictions*, Merseburg, Germany, Apr. 13–16 (1999).
Celik, I., and Y.-Z. Wang, "Numerical Simulation of Circulation in Gas-Liquid Column Reactors: Isothermal, Bubbly, Laminar Flow," *Int. J. Multiphase Flow*, **20**, 1053 (1994).
Delhaye, J., "Jump Conditions and Entropy Sources in Two-Phase Systems," *Int. J. Multiphase Flow*, **1**, 395 (1974).
Delnoij, E., F. A. Lammers, J. A. M. Kuipers, and W. P. van Swaij, "Dynamic Simulation of Dispersed Gas-Liquid Two-Phase Flow Using a Discrete Bubble Model," *Chem. Eng. Sci.*, **52**, 1429 (1997).
Drew, D. A., "Mathematical Modelling of Two-Phase Flow," *Ann. Rev. Fluid Mech.*, **15**, 261 (1983).
Drew, D. A., and R. T. Lahey, Jr., "The Virtual Mass and Lift Force on a Sphere in a Rotating and Straining Inviscid Flow," *Int. J. Multiphase Flow*, **13**(1), 113 (1989).
Drew, D. A., and R. T. Lahey, Jr., "Some Supplemental Analysis Concerning the Virtual Mass and Lift Force on a Sphere in a Rotating and Straining Flow," *Int. J. Multiphase Flow*, **16**(6), 1127 (1990).
Drew, D. A. and S. L. Passman, *Theory of Multicomponent Fluids*, Springer-Verlag, Appl. Math. Sci., New York **135** (1999).
Dudukovic, M. P., F. Larachi, and P. L. Mills, "Multiphase Reactors —Revisited," *Chem. Eng. Sci.*, **54**, 1975 (1999).
Elgobashi, S., and T. Abou-Arab, "A Two-Equation Turbulence Model for Two-Phase Flows," *Physics of Fluids*, **26**, 931 (1983).
Ferziger, J. H., and M. Peric, *Computational Methods for Fluid Dynamics*, 3rd revised ed., Springer-Verlag, Berlin and New York (2002).
Geurst, J. A., "Virtual Mass in Two-Phase Bubbly Flow," *Physica,* **129A**, 233 (1985).
Gosman, A. D., R. I. Issa, C. Lekakou, M. K. Looney, and S. Politis, "Multidimensional Modelling of Turbulent Two-Phase Flows in Stirred Vessels," *AIChE J.*, **38**, 1946 (1992).
Grevskott, S., B. H. Sannaes, M. P. Dudukovic, K. W. Hjarbo, and H. F. Svendsen, "Liquid Circulation, Bubble Size Distribution and Solids Movement in Two- and Three-Phase Bubble Columns," *Chem. Eng. Sci.*, **51**, 1703 (1996).
Harten, A., "High Resolution Schemes for Hyperbolic Conservation Laws," *J. Comput. Phys.*, **49**, 357 (1983).
Hirsch, C., *Numerical Computation of Internal and External Flows*, Volume 2, Wiley, Chichester, U.K. (1990).
Hussaini, M. Y., B. Van Leer, and J. Van Rosendaele, *Upwind and High-Resolution Schemes*, Springer-Verlag, New York (1997).
Hinze, O. J., *Turbulence*, McGraw-Hill, New York (1975).
Issa, R. I., and P. Oliveira, "Modelling of Turbulent Dispersion in Two-Phase Flow Jets," *Engineering Turbulence Modelling and Experiment 2*, Florence, Italy. W. Rodi and F. Martelli, eds., Elsevier, **947**, (1993).
Jakobsen, H. A., B. H. Sanns, S. Grevskott, and H. F. Svendsen, "Modelling of Vertical Bubble-Driven Flows," *Ind. Eng. Chem. Res.*, **36**, 4052 (1997).
Jakobsen, H. A., "Phase Distribution Phenomena in Two-Phase Bubble Column Reactors," *Chem. Eng. Sci.*, **56**, 1049 (2001).
Kaasschieter, E. F., "Preconditioned Conjugate Gradients for Solving Singular Systems," *J. of Comput. Appl. Math.*, **24**, 265 (1988).
Krishna, R., M. I. Urseanu, J. M. van Baten, and J. Ellenberger, "Rise Velocity of a Swarm of Large Gas Bubbles in Liquids," *Chem. Eng. Sci.*, **54**, 171 (1999).
Lathouwers, D., "Modelling and Simulation of Turbulent Bubbly Flow," PhD Thesis, Delft University of Technology (1999).
Mudde, R. F., D. J. Lee, J. Reese, and L.-S. Fan, "The Role of Coherent Structures on the Reynolds Stresses in Two-Dimensional Bubble Columns," *AIChE J.,* **43**, 913 (1997).
Mudde, R. F., and O. Simonin, "Two- and Three-Dimensional Simulations of a Bubble Plume Using a Two-Fluid Model," *Chem. Eng. Sci.,* **54**, 5061 (1999).
Oey, R. S., R. F. Mudde, L. M. Portela, and H. E. A. van den Akker, "Simulation of a Slurry Airlift Using a Two-Fluid Model," *Chem. Eng. Sci.*, **56**, 673 (2001).
Patankar, S. V., "Numerical Heat Transfer and Fluid Flow," Hemisphere Publ. Corp., McGraw-Hill, New York (1980).
Pan, Y., M. P. Dudukovic, and M. Chang, "Numerical Investigation of Gas-Driven Flow in 2-D Bubble Columns," *AIChE J.,* **46**, 434 (2000).
Pfeger, D., S. Gomes, N. Gilbert, and H.-G. Wagner, "Hydrodynamic Simulations of Laboratory Scale; Fundamental Studies of the Eulerian-Eulerian Modelling Approach," *Chem. Eng. Sci.*, **54**, 5091 (1999).
Pfleger, D., and S. Becker, "Modelling and Simulation of the Dynamic Flow Behavior in a Bubble Column," *Chem. Eng. Sci.*, **56** 1737 (2001).
Ranade, V. V., "Modelling of Turbulent Flow in a Bubble Column Reactor," *Chem. Eng. Res. Des.*, **75**, 14 (1997).
Ranade, V. V., and R. P. Utikar, "Dynamics of Gas-Liquid Flows in Bubble Column Reactors," *Chem. Eng. Sci.*, **54**, 5237 (1999).
Saad, Y., "Analysis of Augmented Krylov Subspace Methods," *SIAM J. Matrix Anal. Appl.*, **18**(2), 435 (1997).
Saad, Y., and M. H. Schultz, "A Generalized Minimum Residual Algorithm for Solving Nonsymmetric Linear Systems," *SIAM J. Sci. Stat. Comput.* **7**, 856 (1986).
Sankaranarayanan, K., and S. Sundaresan, "Lift Force in Bubbly Suspensions," *Chem. Eng. Sci.*, **57**, 3521 (2002).
Sokolichin, A., and G. Eigenberger, "Gas-Liquid Flow in Bubble Columns and Loop Reactors: Part I. Detailed Modelling and Numerical Simulation," *Chem. Eng. Sci.*, **49**, 5735 (1994).
Sokolichin, A., and G. Eigenberger, "Applicability of the Standard k-ϵ Turbulence Model to the Dynamic Simulation of Bubble Columns: Part I. Detailed Numerical Simulations," *Chem. Eng. Sci.*, **54**, 2273 (1999).
Tchen, C. M., "Mean Value and Correlation Problems Connected with the Motion of Small Particles Suspended in a Turbulent Fluid," PhD Thesis, Delft University of Technology (1947).
Tennekes, H., and J. L. Lumley, *A First Course in Turbulence*, MIT Press, Cambridge, MA (1942).
Van Leer, B., "Towards the Ultimate Difference Scheme I. The Quest for Monotonicity," *Lect. Notes Phys.*, **18**, 164 (1973).
Van Leer, B., "Towards the Ultimate Difference Scheme II. Monotonicity and Conservation Combined in a Second Order Scheme," *J. Comput. Phys.*, **14**, 361 (1974).
Viollet, P. L., and O. Simonin, "Modelling Dispersed Two-Phase Flows: Closure, Validation and Software Development," *Appl. Mech. Rev.*, **47** (6 part 2), S80 (1994).
Wells, M. R., and D. E. Stock, "The Effect of Crossing Trajectories on the Dispersion of Particles in a Turbulent Flow," *J. Fluid Mech.*, **136**, 31 (1983).
Wen, Y. C., and Y. H. Yu, *Mechanics of Fluidization, Chem. Eng. Prog. Symp. Ser.*, **62**, 100 (1966).
Zhang, D. Z., and A. Prosperetti, "Momentum and Energy Equations for Dispersed Two-Phase Flows and Their Closure for Dilute Suspensions," *Int. J. Multiphase Flow*, **23**, 425 (1997).
Zijlema, M., "Computational Modelling of Turbulent Flows in General Domains," PhD Thesis, Delft University of Technology (1996a).
Zijlema, M. "On the Construction of a Third-Order Accurate Monotone Convection Scheme with Application to Turbulent Flows in General Domains," *Int. J. Numer. Meth.*, **22**, 619 (1996b).

Manuscript received Sept. 5, 2002, and revision received Jan. 8, 2003.